Flow : a study of electron transport through networks of interconnected nanoparticles

Blok, S.

Citation

Blok, S. (2018, July 4). *Flow : a study of electron transport through networks of interconnected nanoparticles*. *Casimir PhD Series*. Retrieved from https://hdl.handle.net/1887/63527

Version:	Not Applicable (or Unknown)
License:	[Licence agreement concerning inclusion of doctoral thesis in the Institutional Repository of the University of Leiden](#)
Downloaded from:	[https://hdl.handle.net/1887/63527](#)

Note: To cite this publication please use the final published version (if applicable).

Cover Page

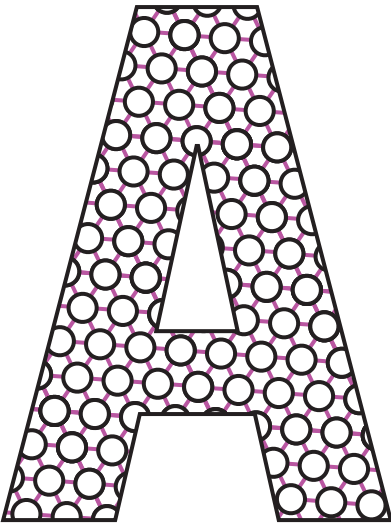**Universiteit Leiden**

The handle http://hdl.handle.net/1887/63527 holds various files of this Leiden University dissertation.

Author: Blok, S.
Title: Flow : a study of electron transport through networks of interconnected nanoparticles
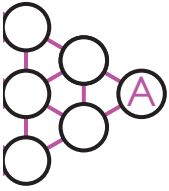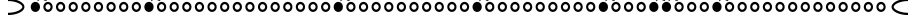**Issue Date**: 2018-07-04

Appendices

Appendix A

Theoretical background of approach 1

Starting from Eq. 3.3, we first take at a look at one of the two possible virtual states. The first virtual state is where an electron from the left lead tunnels through the left molecule onto the nanoparticle. This pathway is finalized by an electron from the nanoparticle that tunnels through the right molecule to the right lead. The matrix element for this state is as follows:

$$\frac{\langle i|\hat{H}|v_1\rangle \langle v_1|\hat{H}|f\rangle}{E_{v_1} - E_i} = \frac{T_{M1}T_{M2}}{E_L - E_{S1} + E_C + eV_L}. \tag{A.1}$$

For the other virtual state, an electron first goes from the nanoparticle through the right molecule to the right lead and is then followed by an electron from the left lead that goes through the molecule onto the nanoparticle. The expression for this process is as follows:

$$\frac{\langle i|\hat{H}|v_2\rangle \langle v_2|\hat{H}|f\rangle}{E_{v_2} - E_i} = \frac{T_{M2}T_{M1}}{E_{S2} - E_R + E_C - eV_R}. \tag{A.2}$$

The initial, virtual and final states are the unperturbed eigenstates of the molecule-nanoparticle-molecule system, defined analogously to the definition used by Averin et al.[Ch. 3, ref 3]. Substituting this back into Eq. A.1, we have to take the occupation of states into account to change the sum over states to a sum over energies. Also rewriting the delta function in terms of the energies in the system, we obtain:

$$\begin{aligned}
\mathcal{R} = \frac{2\pi}{\hbar} \sum_{E_L, E_R, E_{S1}, E_{S2}} &|T_{M1}|^2 |T_{M2}|^2 \\
&\times \left| \frac{1}{E_L - E_{S1} + E_C + eV_L} + \frac{1}{E_{S2} - E_R + E_C - eV_R} \right|^2 \\
&\times f(E_L)\left[1 - f(E_R)\right] f(E_{S2})\left[1 - f(E_{S1})\right] \\
&\times \delta(E_R + E_{S1} - E_L - E_{S2} - eV).
\end{aligned} \tag{A.3}$$

We change the sum for an integral and pragmatically assume:

$$|T_{M1}|^2 |T_{M2}|^2 = T_{M1}(E_L)T_{M2}(E_{S2}) \tag{A.4}$$

to obtain Eq. 3.4. This is done analogously to previous work[Ch. 3, ref 3], where these matrix elements are replaced by constants. To solve this integral numerically, we use the delta function to relate E_R to the other energies ($E_R = E_L - E_{S1} + E_{S2} + eV$) and replace

the four-dimensional integral by a three-dimensional one. We also calculated the current by relating E_L to the other energies ($E_\text{L} = E_\text{R} + E_\text{S1} - E_\text{S2} - eV$) and found no difference between results.

Appendix B

Equivalence of multiple cotunneling model to second-order cotunneling

We start with the Fermi golden rule, just as with normal cotunneling:

$$\mathcal{R}_{i \to f} = \frac{2\pi}{\hbar} |M|^2 \delta(E_f - E_i), \tag{B.1}$$

where E_i and E_f are the initial energy and final energy of the system respectively and M the matrix element for a fourth order cotunneling event. For the model considered by Averin *et al.*[Ch. 3, ref 3], this matrix element can be written as:

$$M = \sum_v \frac{\langle i| \hat{\hat{H}} |v\rangle \, \langle v| \hat{\hat{H}} |f\rangle}{E_v - E_i}, \tag{B.2}$$

whereas for the fourth order cotunneling event, M can be written as:

$$M = \sum_{\{j_1, j_2, j_3, j_4\}} \prod_{k=1}^{3} \frac{\langle v_{k+1}| \hat{H} |v_k\rangle}{E_{v_k} - E_i} \, \langle v_1| \hat{H} |i\rangle . \tag{B.3}$$

The summation is now over 4! virtual states, and the product is over the whole sequence of cotunneling events. In other words, this product can be written as:

$$\prod_{k=1}^{3} \frac{\langle v_{k+1}| \hat{H} |v_k\rangle}{E_{v_k} - E_i} \, \langle v_1| \hat{H} |i\rangle = \frac{\langle i| \hat{H} |v_1\rangle \langle v_1| \hat{H} |v_2\rangle \langle v_2| \hat{H} |v_3\rangle \langle v_3| \hat{H} |f\rangle}{\Delta E_1 \Delta E_2 \Delta E_3}, \tag{B.4}$$

where the energy differences of the Heisenberg uncertainty relation are taken into account by the ΔE_i in the denominator. Following the derivation by Averin *et al.*[Ch. 3, ref 16], we can replace the matrix elements by transmission constants. The previous equation then becomes:

$$\prod_{k=1}^{3} \frac{\langle v_{k+1}| \hat{H} |v_k\rangle}{E_{v_k} - E_i} \, \langle v_1| \hat{H} |i\rangle = \frac{T_1 T_2 T_3 T_4}{\Delta E_{v1} \Delta E_{v2} \Delta E_{v3}}. \tag{B.5}$$

Since the result of multiplication does not depend on the order of multiplication, we can simply write the transmission coefficients as follows:

$$T_1 T_2 T_3 T_4 = T_{L,M1} T_{M1,NP} T_{NP,M2} T_{M2,R}. \tag{B.6}$$

where the transmission coefficients here are respectively from the left lead to the first molecule, from the first molecule to the charging island, from the charging island to the second molecule and from the second molecule to the right lead.

If we assume that the energy differences ΔE_i are dominated by the charging energies of the nanoparticle and molecules, all other energies can be ignored. This means that the sum over all virtual pathways becomes a constant which only depends on the charging energies of the molecules and nanoparticle.
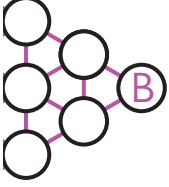
$$\sum_v \frac{T_1 T_2 T_3 T_4}{\Delta E_1 \Delta E_2 \Delta E_3} = \frac{T_{\text{L,M1}} T_{\text{M1,NP}} T_{\text{NP,M2}} T_{\text{M2,R}}}{E_S(E_{\text{C,M1}}, E_{\text{C}}, E_{\text{C,M2}})},$$

$$E_S(E_{\text{C,M1}}, E_{\text{C}}, E_{\text{C,M2}}) \equiv \left(\sum_v \frac{1}{\Delta E_{v1} \Delta E_{v2} \Delta E_{v3}} \right)^{-1}.$$

(B.7)

If we now define $T_1^\dagger \equiv T_{\text{L,M1}} T_{\text{M1,NP}}$ and $T_2^\dagger \equiv T_{\text{NP,M2}} T_{\text{M2,R}}$, we have:

$$M = \frac{T_1^\dagger T_2^\dagger}{E_S},$$

(B.8)

which is similar to the matrix element in cotunneling derived by Averin *et al.*[Ch. 3, ref 16]. This therefore means that our fourth order cotunneling event will resemble the already familiar cotunneling, with a transmission function that decreases with increasing Coulomb charging energy. This in turn means that even if there are single levels in between the charging island and the leads, the transmission probability of these levels will be constants.
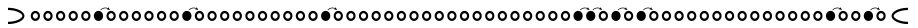
Appendix C

Pulse tube operation

The Oxford Instruments Teslatron is a closed loop cryostat, which means that it uses a compression/decompression cycle in a pulse tube to cool down the sample. A typical pulse tube is shown in Fig. C.1. In the beginning of the compression cycle, the piston moves downwards, increasing the pressure of the gas and forcing it to flow through the regenerator, heating it. The flow continues through the cold end of the pulse tube (T_C) to the hot end (T_H). The hot end is kept at room temperature, and the compressed gas is cooled down at the end of the compression cycle (Fig. C.1 center image). During the decompression cycle (Fig. C.1 right image), the gas in the pulse tube expands, causing it to cool down. The cool gas cools down the heat exchanger at the cold end and enters the regenerator. Here, the regenerator exchanges heat with the cold gas, causing it to cool down to a lower temperature than in the previous cycle. Since the regenerator pre cools the gas before compression the cold end of the pulse tube iteratively achieves a lower temperature. In most systems, the gas on the hot end of the pulse tube does not reach the cold end, which thermally insulates both ends.

The Teslatron uses a two-stage pulse tube cooler to achieve its base cold stage temperature of 3 K. This means that a second pulse tube and regenerator are added to the loop. The first pulse tube and regenerator cool a stage down to between 70 and 40 K, which is used to pre-cool the second stage. Although Fig. C.1 shows a piston to act as a compressor, no piston is used in the cryostat. Instead, an external 7.5 kW compressor compresses and pre-cools the helium back to room temperature. The high pressure (20 bars) helium is fed
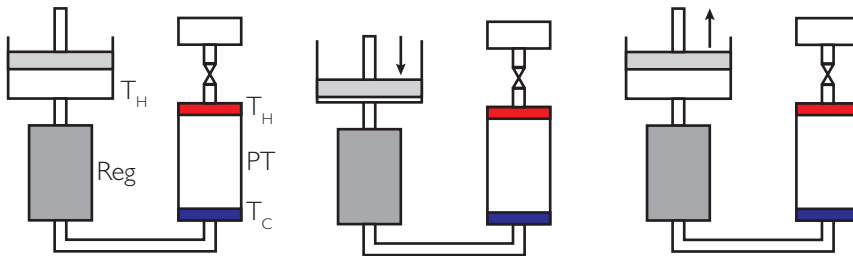
Fig. C.1: Schematic of a pulse tube cooler during various stages of the cooling cycle. Left is before the compression cycle, center is after the compression cycle, right is after the decompression cycle, seen as a difference in position of the piston. Each cycle iteratively cools down the regenerator (Reg), by repeatedly compressing and expanding the gas in the pulse tube (PT).
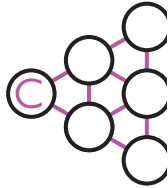
into the cryostat using a rotary valve to control the flow. This valve periodically switches between the high and low pressure lines of the compressor

In order to cool down to even lower temperatures, the 3 K stage is used to cool down a helium gas flow. The helium exchanges heat with the stage, causing it to cool down. By pumping on the other side of the helium, the helium expands and cools down even further. It then flows past the insert chamber, cooling down the chamber and the insert inside of it. By varying the flow of the helium using a needle valve, the cooling power can be regulated. A lower flow gives a lower pressure, causing the helium to cool down more. However, since the helium pressure is low, the amount of helium flowing past the insert chamber is also low, causing a low cooling power. Increasing the helium flow increases the cooling power, but raises the helium temperature. Therefore, in order to cool down quickly, the insert is first cooled down to 50 K at high helium flow, after which the flow is reduced in order to reach base temperature.

It is worthwhile to note that the bottom of the insert is physically separated from the insert chamber. In order to allow heat to flow from the insert to the chamber walls, the insert chamber is filled with room pressure helium exchange gas before cooling down. In order to increase heat exchange at low temperatures, extra helium is added at low temperature*.

---

*Due to the ideal gas law, a volume of room pressure gas at low temperatures will build up a high pressure when heated up. It is therefore important that a properly working overpressure valve is fitted to the insert chamber.
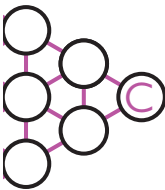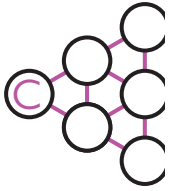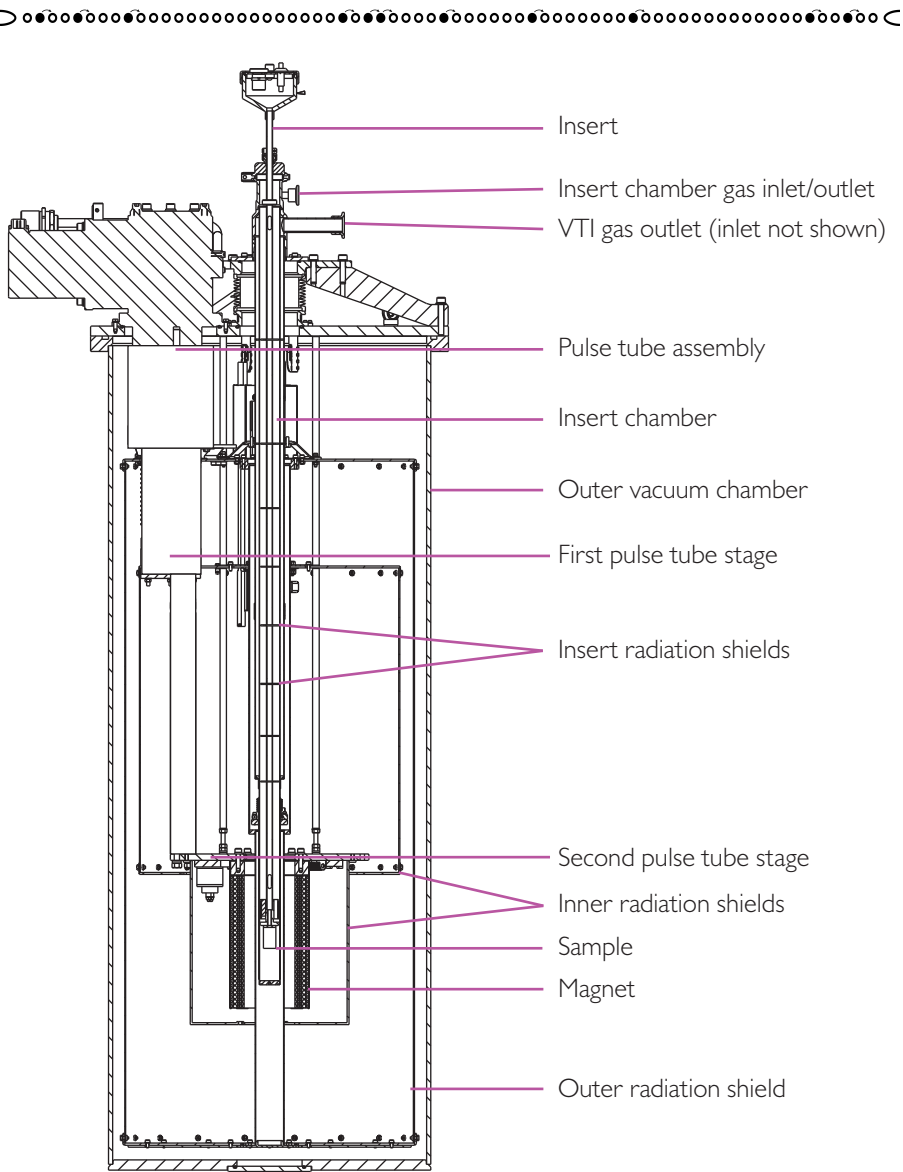
Fig. C.2: Schematic of the Teslatron cryostat as delivered by Oxford Instruments. The bulk of the machine is made up by the outer vacuum chamber providing thermal solation from the environment. The placement of the two stage pulse tube and the attachment to the radiation shields can be clearly seen in this figure.

Appendix D

Exploring the parameter space of the alternative model

In order to determine whether the correlation between the slope and the average cotunneling length, we explore more of the parameter space by varying E_C and $G_{\mathcal{T}}$. We repeat the calculation for 30 values of the transmission probability $G_{\mathcal{T}}/G_0$ and 30 values of E_C, each for 25 temperatures (22 500 IV-curve calculations for 11 250 000 total data points). Since 22 500 IV-curves are too many to analyze individually, we determine j_{mean} and the slope at each data point and correlate them in a histogram. The results can be seen in Fig. D.1, which shows the logarithm of the number of occurrences of each combination of j_{mean} and slope. The logarithm is taken, since a large part of the IV-curves are sequential tunneling (CI and CIII regimes) and push the rest of the histogram off of the scale.
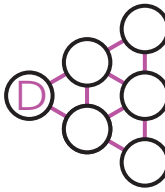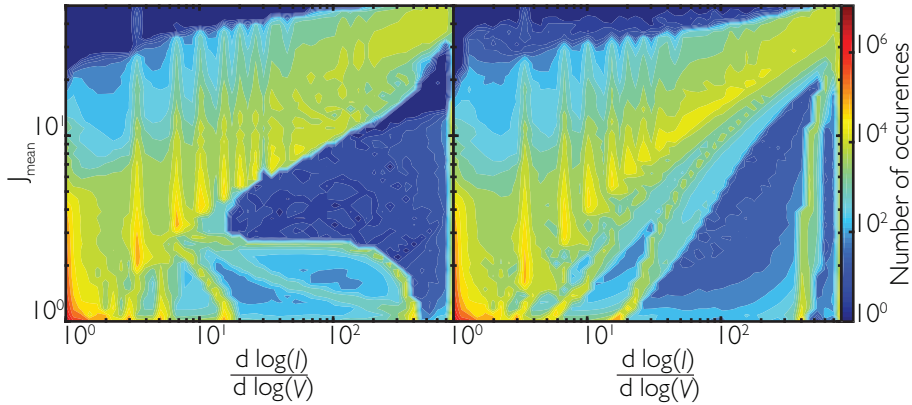
Fig. D.1: Histogram showing the number of occurrences for each combination of j_{mean} and slope, colormap is on a logarithmic scale. Left is the model using the alternative model in Eq. 5.13, right replaces the probability term $\mathcal{P}$ from Eq. 5.12 by the term in Eq. 5.10, effectively removing the dependence on cotunneling length of E_C. Removing this dependence slightly decreases the cotunneling length for all systems, seen as the general downward shift of the green graph. Otherwise, the graphs look similar. It can be seen that as the slope increases, so does the cotunneling length. However, certain values of slope (e.g. 3.5, 7, 10) correspond to many values of average cotunneling length. We think this might have something to do with the sharp steps in j_{mean} corresponding to peaks in the slope, as seen in Fig. 5.4, but the exact origin of this is unclear.

The graphs show that although no one-to-one correspondence is present, there is a correlation between the slope and j_{mean} in both diagrams. Interestingly, there are certain values of slope which occur more often than others and correspond to a range of j_{mean}. Although the origin of these features is unclear, they might have to do with the stepwise increase in j_{mean} correlating with peaks in the slope, seen in Fig. 5.4.

Since the prediction of the Arrhenius model that j_{mean} depends on the slope is only an approximation valid in a certain regime, it makes sense to compare the results in Fig. D.1 to the same calculation using the Arrhenius model. These can be seen in Fig. D.2.
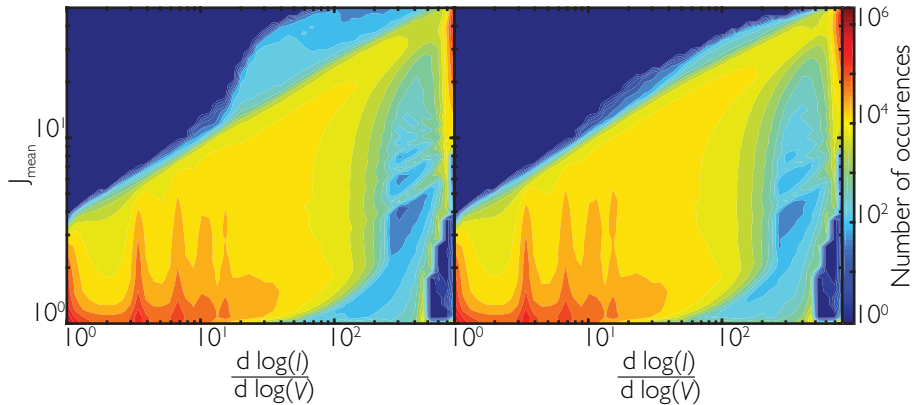
Fig. D.2: Histogram showing the number of occurrences for each combination of j_{mean} and slope, calculated with the Arrhenius model. Left is the model using Eq. 5.1, but replaced the probability term by Eq. 5.12, left is calculated using Eq. 5.1. The left therefore has a reduction in E_{C}, and the right one has not, identical to Fig. D.1. Using the reduction in E_{C} slightly increases the cotunneling length in cases of high slope. The graphs are smoother than those in Fig. D.1, indicating less preference for certain values of slope. Otherwise, there is a wide distribution in j_{mean} and slope, similar to the previous graph.

Although the general structure is similar to Fig. D.1, there are some striking differences. The first is that the predicted cotunneling length according to the Arrhenius model is lower than according to the new model. Furthermore, the graphs are more smoothed out than Fig. D.1, which have more detailed features. This means that there are no preferred values for slope, such as in the previous model, nor are there preferred cotunneling lengths. Otherwise, the graphs have the same structure, indicating that the overall correlation between j_{mean} and the slope is similar in both models across all regimes. It should be noted that these figures show data across all regimes, not only the C2 regime.

We further investigated both models in the C2 and CII regimes, so see if the link between slope and j_{mean} is more clear here. The results are shown in Fig. D.3.
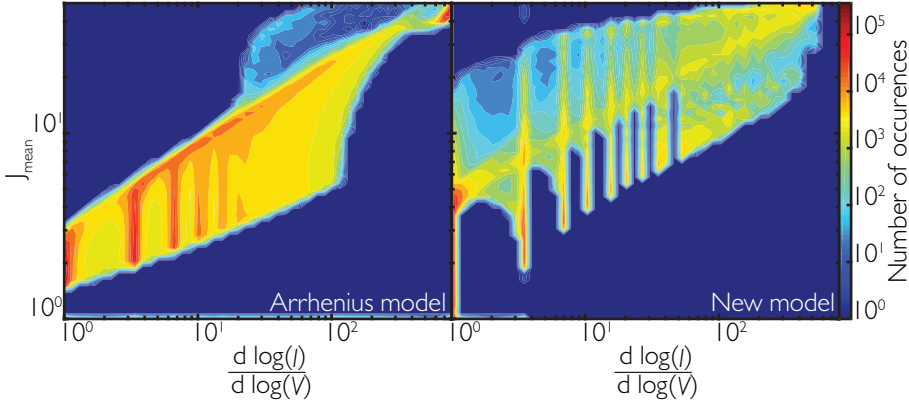
Fig. D.3: Histogram showing the number of occurrences for each combination of j_{mean} and slope, calculated with the Arrhenius model (left) and the new model (right). The Arrhenius model shows a much stronger correlation between j_{mean} and slope in the C2 regime, although there are still a lot of possible values for j_{mean} for each value of slope. The New model shows an even more peculiar pattern. Certain values of slope are preferred, which correspond to many different average cotunneling lengths.
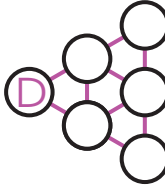
Comparing these figures to the previous calculations, we see that there is less freedom in j_{mean} for each value of slope. However, there are still many possible values for j_{mean} at each slope, especially for the new model. Moreover, the new model shows that certain slopes have a very high occurrence rate, with those in between almost not happening at all. These features can also be seen in Fig. D.1. We think that these have the same origin, and the values in between the preferred slopes fall outside the CII regime.

From these data, we conclude that in both models, but especially in the new model, the correlation between j_{mean} and slope is non-trivial. Specifically, it is not generally possible to determine j_{mean} from α.
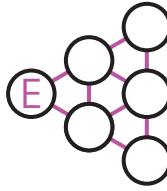
Appendix E

Additional data for chapter 6

E.1 ADDITIONAL FITTING ON 10 NM NANOPARTICLE NETWORKS

In addition to the data shown in Fig. 5.8, we show that a different device on the same sample can be fitted using the new model. We fit the model to the data before and after exchange, as can be seen in Fig. E.1. The model follows the pre-exchange data nicely, although it predicts a current that is too low at around 0.1 V. This underestimation is less present in the post-exchange data. Moreover, the model gives an accurate fit to the post-exchange data, only needing a significant change in $G_{\mathcal{T}}$ (around four orders of magnitude) and E_{C} and $E_{\mathrm{C,var}}$ (a factor of two). The rest of the fitted parameters are almost identical.

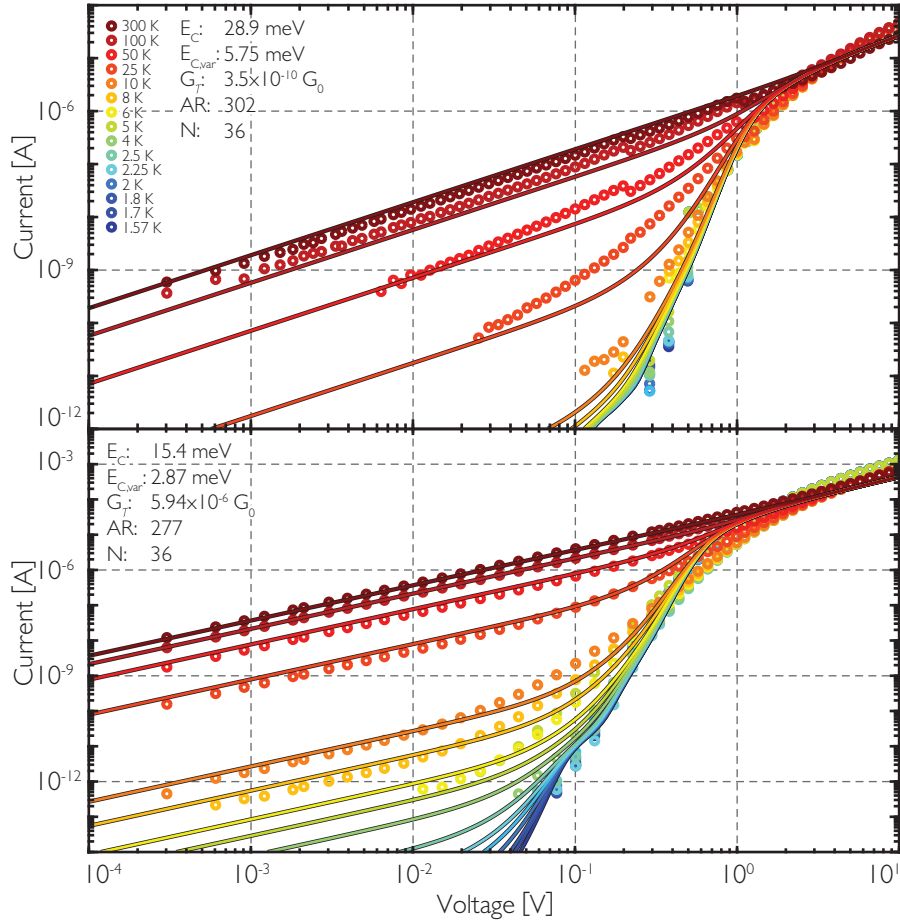|	E_{C}	$E_{\mathrm{C,var}}$	$G_{\mathcal{T}}$	AR	N
Pre exchange	28.9 meV	5.75 meV	$3.50{\cdot}10^{-10}$ G_0	302	36
Post exchange	15.4 meV	2.87 meV	$5.94{\cdot}10^{-6}$ G_0	277	36

Fig. E.1: Pre-exchange (top) and post-exchange (bottom) current versus voltage plots with the corresponding fitted curves using the new model. The data is of a different device on the same sample as the data from Fig. 5.8. The fits show the same trend as in chapter 5, with the pre-exchange fit being slightly too low around 0.1 V, a feature which is less present post exchange. The parameters before and after exchange are similar to those in chapter 5, with the exception of the post-exchange $G_{\mathcal{T}}$ being an order of magnitude lower in this device. Additionally, the post-exchange E_C is 25% smaller in this device, which is half the pre-exchange value.
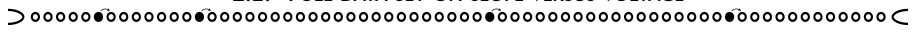
E.2 FULL DATA SET ON SLOPE VERSUS VOLTAGE

Fig. E.2: The original data from Fig. 5.10, including the data removed in this figure. For a complete description, see Fig. 5.10 in chapter 5.
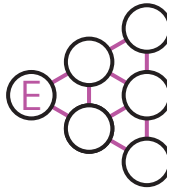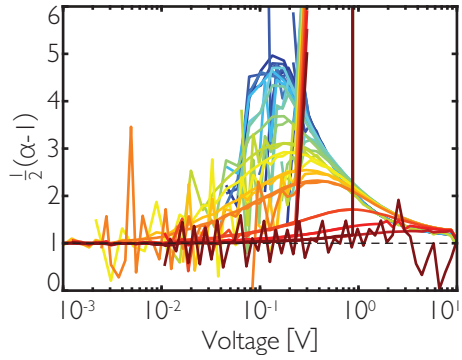
Appendix F

Fits to the data after exchange with molecular switches

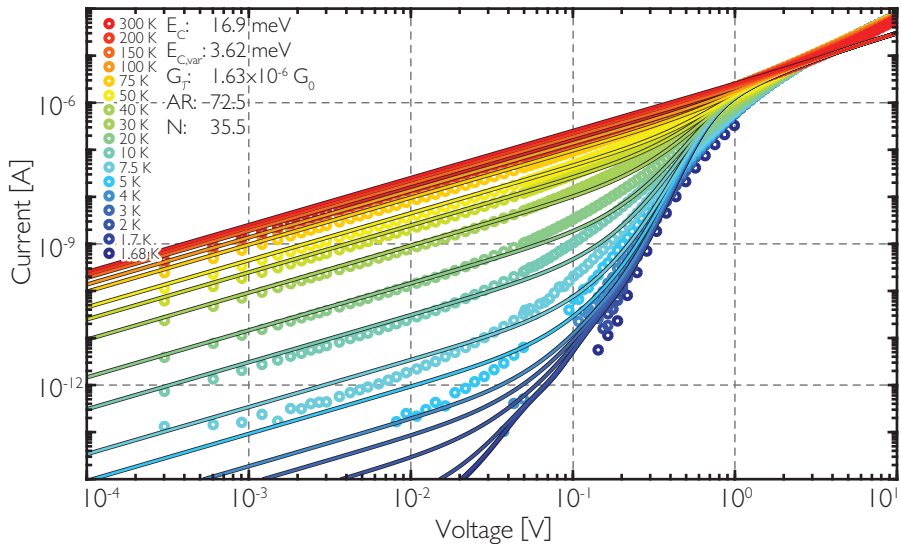The figure below shows the fits to the data obtained in chapter 6.

Fig. F.1: Fits to the data in Fig. 6.8 using the new model. The parameters are similar to those found in chapter 5, although E_C is around twenty percent lower.